

Effect of Environmental Screening and Strain on Optoelectronic Properties of Two-Dimensional Quantum Defects

Shimin Zhang and Kejun Li

Department of Physics, University of California, Santa Cruz, CA, 95064, USA

Chunhao Guo and Yuan Ping*

Department of Chemistry and Biochemistry, University of California, Santa Cruz, CA, 95064, USA

(Dated: April 13, 2023)

Point defects in hexagonal boron nitride (hBN) are promising candidates as single-photon emitters (SPEs) in nanophotonics and quantum information applications. The precise control of SPEs requires in-depth understanding of their optoelectronic properties. However, how the surrounding environment of host materials, including number of layers, substrates, and strain, influences SPEs has not been fully understood. In this work, we study the dielectric screening effect due to the number of layers and substrates, and the strain effect on the optical properties of carbon dimer and nitrogen vacancy defects in hBN from first-principles many-body perturbation theory. We report that the environmental screening causes lowering of the GW gap and exciton binding energy, leading to nearly constant optical excitation energy and exciton radiative lifetime. We explain the results with an analytical model starting from the BSE Hamiltonian with Wannier basis. We also show that optical properties of quantum defects are largely tunable by strain with highly anisotropic response, in good agreement with experimental measurements. Our work clarifies the effect of environmental screening and strain on optoelectronic properties of quantum defects in two-dimensional insulators, facilitating future applications of SPEs and spin qubits in low-dimensional systems.

I. INTRODUCTION

Point defects in two-dimensional (2D) materials emerge to possess outstanding quantum properties such as stable single-photon emission, and have been exploited as spin quantum bits (qubits) for quantum information technologies [1, 2]. The single photon emitters (SPEs) in 2D materials are highly stable and tunable [2–4], and in particular, their optical activation can be spatially controlled and tuned by strain [5, 6], emphasizing the great potential of SPEs in 2D materials.

The defect candidates with promising quantum properties exhibit deep-level states or form defect-bound exciton. A large number of defects in hBN have been proposed since the report by Tran et al. [7]. So far, spin defect V_B^- has been unambiguously identified from experiment [8–11] and theory [12, 13]. Many of the other defects, whose atomic origins are yet to be determined, were found to be ~ 2 eV and ~ 4 eV SPEs [14–17]. From theoretical predictions, $N_B V_N$ [7, 14], boron dangling bonds [18], $C_B V_N$ [19, 20], and carbon trimers [21–24] were proposed to be defect candidates for the ~ 2 eV SPEs, while $C_B C_N$ [25], $C_N O_N$ [26], Stone-Wales defect [27], and carbon ring [28] were for the ~ 4 eV SPEs.

Among the proposed defect candidates, only partial experimental observations can be explained. Most importantly, large variations of key physical properties including Zero-Phonon Line (ZPL), photoluminescence (PL) lifetime, and Huang-Rhys (HR) factor [22, 29] were observed. The physical origin of such variation is undeter-

mined, with only some plausible explanations. For example, it is speculated that different substrates or sample thickness used in experiments may lead to variation [7, 15, 30]. Strain can be another source for the variation, as indicated by the past experimental studies [14, 31, 32]. Natural strain can be introduced when placing materials on top of substrates.

Theoretically, first-principles computation has been a powerful tool for identifying and proposing new defects as SPEs and spin qubits in 2D materials [33]. However, different structural models including monolayer, multilayer or bulk hBN [13, 21–25] were used in different studies, which lead to difficulties of comparing with experiments and comparison among different theoretical studies. Furthermore, the effect of substrates has been mostly examined at the mean-field level by DFT with semilocal functionals, where excitonic effects are not considered [34–36]. At last, the effect of strain on optical properties such as absorption spectra, exciton binding energies, and radiative lifetime has not been investigated to our best knowledge.

In this work, from first-principles calculations, we investigate the environmental screening effect due to the layer thickness and substrates, as well as the strain effect on the optoelectronic properties of point defects in hBN. In order to pick representative defects for general conclusions, we choose $C_B C_N$ as an example of extrinsic substitutional defects and $N_B V_N$ as an example of native vacancy defects, both of which were commonly found in hBN and previously proposed to be possible ~ 4 eV and ~ 2 eV SPEs respectively. Our results provide an estimation on how sensitive the excitation energy, exciton binding energy, and ZPL are to strain, and we explain their qualitative trends through molecular orbital the-

* yuanping@ucsc.edu

ory. We also provide intuitive and comprehensive understanding of environmental screening effect on defect properties through both first-principles many-body perturbation theory calculations and analytical models.

II. COMPUTATIONAL METHOD

The ground state calculations are carried out by density functional theory implemented in QuantumEspresso package[37], with the Perdew-Burke-Ernzerhof (PBE) exchange correlation functional [38]. We use the SG15 Optimized Norm-Conserving Vanderbilt (ONCV) pseudopotentials [39, 40] and 80 Ry wave function kinetic energy cutoff (320 Ry charge density cutoff) for plane wave basis set. The defect calculations are performed with 6×6 supercell and $3 \times 3 \times 1$ k-point sampling, based on our convergence tests in previous studies [22, 31, 41].

We perform the many-body perturbation theory calculations with G_0W_0 starting from PBE electronic states for the quasi-particle energies, and solve the Bethe-Salpeter equation (BSE) for the optical properties [42] with excitonic effects by the Yambo-code [43]. The GW calculation is carried out with 8 Ry response block size and 1800 energy bands for the dielectric matrix and self-energy, while we use 5 Ry and 80 bands for the BSE kernel and optical spectra calculations. With the 2D Coulomb truncation technique [44], the quasi-particle energies are converged within 10 meV at 33.5 a.u. vacuum size. More details on convergence tests can be found in SI Fig.S1 and Fig.S2.

We then calculate the ZPL by subtracting the Frank-Condon shift E_{FC} from the BSE excitation energy, where the E_{FC} is obtained by the constrained DFT (cDFT) technique [41]. By taking the excitation energy and exciton dipole moment from the solution of BSE, we then evaluate radiative lifetime for defects in 2D systems derived from the Fermi's golden rule, with $\tau_R = 3\pi\epsilon_0\hbar^4 c^3 / n_D e^2 E^3 \mu^2$ [41, 45]. Here E is the exciton energy, c is the speed of light, μ^2 is the modulus square of exciton dipole moment, and n_D is reflective index, which is one for monolayer hBN.

For the study of layer thickness and substrate effects, we apply our recently-developed sum-up effective polarizability ($\chi_{\text{eff-sum}}$) with the reciprocal-space linear interpolation technique, in order to account for the impact of substrates and multilayers[46, 47]. This method allows us to separate the total interface into two subsystems as substrate pristine layers and defective monolayer, allowing a large saving of computational cost and avoiding artificial strain from enforcing lattice matching at interfaces.

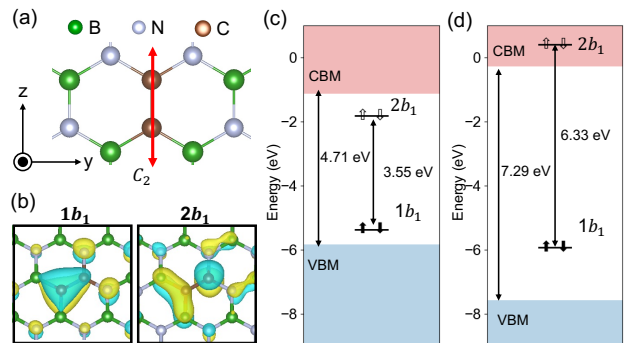


FIG. 1: Structural and electronic properties of carbon dimer ($C_B C_N$) in hBN. (a) Atomic structure, (b) defect-related wave functions, and the single-particle diagram of ground state at the level of (c) PBE and (d) $G_0W_0@PBE$. The zero energy is aligned to the vacuum level, and the defect states are labeled by their wave function symmetry based on the irreducible representation of C_{2v} symmetry group.

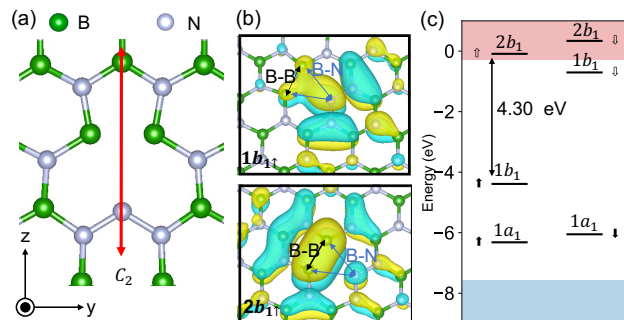


FIG. 2: Structural and electronic properties of nitrogen vacancy ($N_B V_N$) in hBN with C_{2v} symmetry. (a) Atomic structure, (b) defect-related wave functions, and (c) single-particle diagram of ground state at $G_0W_0@PBE$ level. The vacuum level and defect state notations are set up in the same way as $C_B C_N$.

III. RESULTS AND DISCUSSIONS

A. Electronic and Optical Properties of Defects in hBN

We start from the discussion of electronic structure and optical properties of defects in monolayer hBN at natural lattice constant, then followed by the discussion of strain and layer thickness/substrate effects. We choose carbon dimer ($C_B C_N$) and nitrogen vacancy ($N_B V_N$) defects in hBN as our prototypical systems, both of which are common defects in hBN. In particular $C_B C_N$ was identified as a defect candidate for 4 eV SPE in hBN [48]. The atomic structures and electronic

structures of $C_B C_N$ and $N_B V_N$ are shown in Fig. 1 and Fig. 2, respectively. The atomic structure shows that both $C_B C_N$ and $N_B V_N$ belong to the C_{2v} point symmetry group. We label the defect wave functions according to the irreducible representations to which they transform. In particular, the $1b_1$ and $2b_1$ states of $C_B C_N$, and $1b_{1\uparrow}$ and $2b_{1\uparrow}$ states of $N_B V_N$ are of interest, as they correspond to the optically allowed intra-defect transitions [48, 49]. The comparison between the electronic structures at PBE and $G_0 W_0 @ PBE$ levels in Fig. 1c and d indicates that the quasiparticle correction shifts the occupied defect states downward and unoccupied states upward, opening up the defect gap of $C_B C_N$ to 6.33 eV from 3.55 eV, and the defect gap of $N_B V_N$ to 4.30 eV from 2.06 eV at PBE.

We then carried out BSE calculations for the related vertical excitation energy. The complete BSE spectra and the exciton wave function are presented in the SI Figs. S3 and S4. The results of $C_B C_N$ indicate the presence of a single isolated peak related to the $1b_1 \rightarrow 2b_1$ transition at the BSE excitation energy (E_{BSE}) of 4.44 eV, with a corresponding exciton binding energy of 1.89 eV and a radiative lifetime of 1.1 ns. The zero-phonon line energy (E_{ZPL}) was calculated to be 4.32 eV by subtracting the Frack-Condon shift (E_{FC}) of 0.12 eV from the BSE excitation energy. This result is in agreement with previous studies, where a ZPL around 4.3 eV has been obtained using cDFT with hybrid functional [48] or GW&BSE with a finite-size cluster approach [50]

We acknowledge the intricate nature of local structural distortion and optical transition of the $N_B V_N$ defect, and the related detailed discussion is presented in the SI section III. However, to keep the main text concise, we focus on the $1b_{1\uparrow} \rightarrow 2b_{1\uparrow}$ transition at C_{2v} defect symmetry. The vertical transition energy for $1b_{1\uparrow} \rightarrow 2b_{1\uparrow}$ is 2.12 eV with a 57 ns radiative lifetime. The ZPL is 1.60 eV after subtracting the E_{FC} 0.52 eV from the vertical transition at BSE. Upon considering the transition to the lower symmetry ground state at C_s symmetry due to out-of-plane distortion, the ZPL energy increases to 1.70 eV. Our result for $1b_{1\uparrow} \rightarrow 2b_{1\uparrow}$ transition related ZPL is lower than the previous calculation [5, 51] at hybrid functional, but consistent with previous BSE results at the same structure [52]. This highlights the important difference when excitonic effect is taken into account.

B. Effect of Strain

We investigate the effect of strain by applying it along two in-plane uniaxial directions, where the parallel (\parallel) strain denotes the strain along the C_2 axis, and the perpendicular (\perp) strain denotes the direction perpendicular to the C_2 axis. The uniaxial strain here is defined as the stretching ratio of the lattice along a certain direction, with its magnitude as $\epsilon = (l - l_0)/l_0$, where l_0 and l are the lattice lengths before and after the strain

is applied. ϵ denotes the macroscopic strain on the entire system. The strain tensor can thus be written as $\epsilon_{i,j} = \epsilon \cos\theta_i \cos\theta_j$ [6] where θ_i (θ_j) is the angle between strain axis and i^{th} (j^{th}) coordinate direction (as defined in Fig. 1(a) and Fig. 2(a)).

Due to the C_{2v} symmetry, the response of ZPL to the applied strain at the first order depends only on two in-plane diagonal components of the strain tensor, and thus can be written as:

$$\Delta E_{ZPL} = \epsilon(\kappa_{\parallel} \cos^2\theta + \kappa_{\perp} \sin^2\theta), \quad (1)$$

where θ is the angle between the strain axis and C_2 axis. The energy response to strain is quantified by two linear strain susceptibilities $\kappa_{\parallel(\perp)}$. In order to understand the determining factors on ZPL energy change (ΔE_{ZPL}) when applying strain, ΔE_{ZPL} can be decomposed into different contributions as follows.

$$\Delta E_{ZPL} = \Delta E_{PBE} + \Delta E_{QP} - \Delta E_b - \Delta E_{FC}, \quad (2)$$

where ΔE_{PBE} is the change of DFT single particle energy at the PBE level due to strain; ΔE_{QP} is the change of quasiparticle energy correction; ΔE_b is the change of exciton binding energy by solving BSE, and ΔE_{FC} is the change of excited state relaxation energy (Frack-Condon shift) under strain.

We thus can separate ZPL's strain susceptibility (κ_{ZPL}) into terms corresponding to different levels of contribution from Eq. 2,

$$\kappa_{ZPL}^{\parallel(\perp)} = \kappa_{PBE}^{\parallel(\perp)} + \kappa_{QP}^{\parallel(\perp)} - \kappa_b^{\parallel(\perp)} - \kappa_{FC}^{\parallel(\perp)}. \quad (3)$$

By providing all the strain susceptibility components in Eq. 3, we can reveal the origin of ZPL response to strain.

The effect of strain on the structural, electronic, and optical properties of $C_B C_N$ in monolayer hBN is described in Fig. 3. Fig. 3(a) displays the change in three bond lengths, including the defect-defect bond length (C-C) and the defect-nearest-neighbor bond lengths (C-N and C-B). All three bond lengths increase linearly with strain (where a positive sign denotes stretching strain and a negative sign denotes compressing strain). Fig. 3(b) illustrates the change in defect electronic energy gap at PBE level (E_{PBE}) and $G_0 W_0 @ PBE$ level (E_{GW}). Fig. 3(c) and (d) present the optical properties of the defect emitter, including the absorption peak related to $1b_1 \rightarrow 2b_1$ transition at RPA and BSE levels (c), and the corresponding BSE excitation energy (E_{BSE}), ZPL (E_{ZPL}), and exciton binding energy (E_b) as a function of strain (d). Both the optical and electronic energy gaps of the defect-related transition exhibit a linear red shift with increasing strain, with the parallel strain resulting in a larger response compared to the perpendicular strain. However, the radiative lifetime (τ_R) and exciton binding energy (E_b) show negligible response to the strain.

The linearity of response to strain in Fig. 3 suggests that the linear response model represented by Eq. 1 and

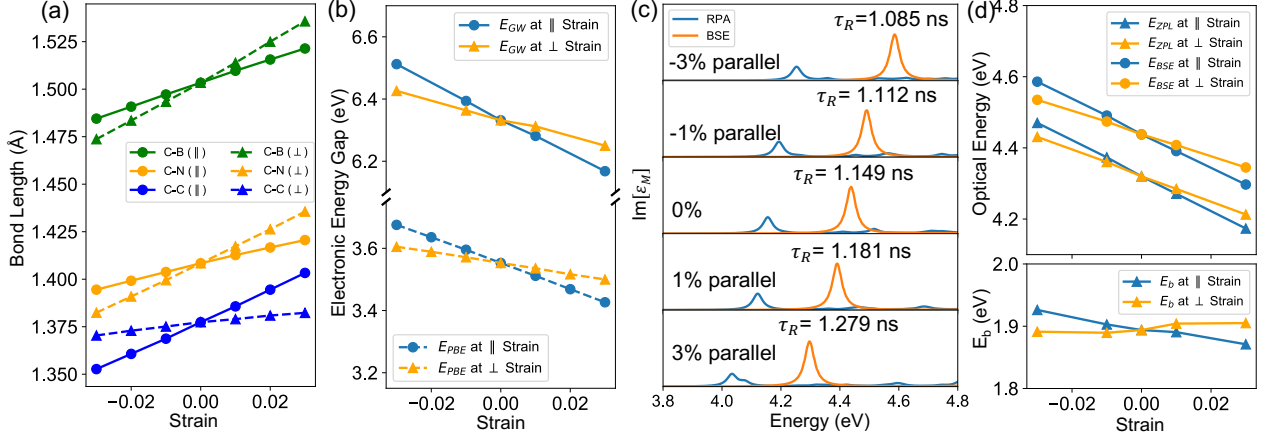


FIG. 3: Strain effect on electronic and optical properties of $1b_1 \rightarrow 2b_1$ transition at $C_B C_N$ in hBN. (a) Bond length change of the $C_B C_N$ defect as parallel (to C_2 symmetry axis, \parallel) and perpendicular (\perp) strain is applied. (b) Electronic energy gap change between defect states, including PBE and GW@PBE results along two directions of strain. (c) Optical spectra (only energy range below the bulk-state transition shown) are red shifted as the strain increases at both RPA level (blue) and BSE level (orange). The radiative lifetime is denoted as τ_R . (d) BSE excitation energy and ZPL energy (up), exciton binding energy (E_b , down).

TABLE I: The bond length change rate (R) and strain susceptibilities (κ , with unit of meV/%) of $C_B C_N$ and $N_B V_N$ under the parallel (\parallel) and perpendicular (\perp) strain. The subscript of R denotes the atomic distance/chemical bond of interest, surrounding the defect center. The subscript of κ represents various contributions, i.e. “QP” denotes quasiparticle correction; “b” denotes exciton binding energy; “FC” denotes Frank condon shift; “ZPL” denotes zero-phonon lines.

		$C_B C_N$						
	R_{C-C}	R_{C-B}	R_{C-N}	κ_{PBE}	κ_{QP}	κ_b	κ_{FC}	κ_{ZPL}
\parallel	0.613	0.301	0.411	-41.58	-15.70	-8.90	1.30	-49.63
\perp	0.144	0.629	0.688	-17.75	-11.40	2.82	4.64	-36.49
		$N_B V_N$						
	R_{B-B}	R_{B-N}	-	κ_{PBE}	κ_{QP}	κ_b	κ_{FC}	κ_{ZPL}
\parallel	0.463	1.664	-	-59.70	-19.32	-14.27	40.35	-105.20
\perp	2.072	0.490	-	44.96	1.00	2.05	6.31	38.02

Eq. 3 is adequate. As a result, the strain susceptibility and bond length change rate (R_ν ; related to the local bond length change speed under strain, will be defined later) are summarized in TABLE I. Similar calculations were performed for the $N_B V_N$ defect system, summarized in the same table as well.

The results of ZPL strain susceptibility (κ_{ZPL}) reveal that the $C_B C_N$ defect exhibits a similar negative strain susceptibility (red shift of ZPL) in both \parallel and \perp components, i.e. $\kappa_{ZPL}^\parallel = -49.63$ meV/% and $\kappa_{ZPL}^\perp = -36.49$ meV/%. On the other hand, the $N_B V_N$ defect exhibits a disparate strain response behavior in two directions, where the \parallel component of strain susceptibility is negative ($\kappa_{ZPL}^\parallel = -105.20$ meV/%) and the \perp component is positive ($\kappa_{ZPL}^\perp = 38.02$ meV/%). The sign difference on strain susceptibility reflects the different bonding nature of defects as discussed later. By substituting the two components of strain susceptibilities into Eq. 1, one

can determine the ZPL energy shift under any uniaxial strain in the linear response regime. Previous experimental work has shown that the uniaxial strain susceptibility of 2 eV SPE ranges from -120 meV/% to 60 meV/% without specifying the strain direction [6, 53, 54]. Therefore, our calculated strain response for the $N_B V_N$ defect falls within the experimental strain susceptibility range [55] (more related discussion detailed in SI).

Our analysis of κ_{ZPL} composition in Table I indicates that the determining factors of strain response is different between two defect systems. For $C_B C_N$ defect, the change from single-particle level at PBE and GW (κ_{PBE} and κ_{QP}) has the dominant contribution, while exciton binding energy κ_b and the Frank-Condon shift κ_{FC} have a negligible impact. On the other hand, for the $N_B V_N$ defect, although κ_{PBE} and κ_{QP} still dominate, the other contributions from κ_b and κ_{FC} have a sizable impact for κ_{ZPL}^\parallel (not for κ_{ZPL}^\perp). Our analysis of the strain susceptibility highlights the importance of many-body effects and

excited-state relaxation in determining the optical strain response. These factors impact both the magnitude and anisotropy of the response. In light of these findings, it is crucial to consider these effects in the study of strain engineering for optical spectroscopy.

We then discuss the bond length change rate (R_ν) of local atomic distance ν (TABLE I) to identify the most relevant molecule orbitals responding to strain. The bond length change rate is defined as $(d_\nu - d_{0\nu})/(d_{0\nu})$, with $d_{0\nu}$ and d_ν as the local atomic distances before and after applying the strain. This quantity indicates to what extent the macroscopic tensile/compression strain can be transferred into the microscopic local structural change. This helps us develop insights on optoelectronic properties based on molecular orbital theory, given the localized nature of defect-related wave functions.

For example, in the $C_B C_N$ defect system, C-C bond has the largest change under the parallel (\parallel) strain to C_2 axis (therefore the largest R_{C-C}), which induces change to the corresponding molecular orbitals (MO) between two carbon atoms. From the defect wavefunctions in Fig. 1b, we can find the lower defect level $1b_1$ has a π bonding character between two C atoms; instead, the higher defect level $2b_1$ has a π^* antibonding character. As a result, the stretching of the C-C bond weakens charge density overlap between two C atoms, leading to a decrease of energy gap between π ($1b_1$) and π^* ($2b_1$), shown as a red shift in Fig.3(b) and (c). This change also results in a negative strain susceptibility in Table I. Similar discussions can be applied to the $N_B V_N$ defect system as well; one exception is that the strain susceptibility is positive when applying strain perpendicular to the C_2 axis of $N_B V_N$ defect, where we found the B-B distance has the largest change (R_{B-B} close to 1). Interestingly, the highest occupied defect level $1b_1$ has a nearly non-bonding character between two B atoms, but the lowest unoccupied defect level $2b_1$ in the same spin channel has a bonding character between two B atoms. Stretching B-B bond will decrease the charge density overlap between two B, which increases the energy of $2b_1$ but weakly affects $1b_1$. As a result, the energy gap between two defect levels is increased, which explains its positive κ along \perp direction, opposite to the others in Table I.

In summary, our study analyzed the effects of strain on the electron and optical properties of hBN defects through the use of two representative systems: the carbon-dimer defect $C_B C_N$ and the nitrogen vacancy complex $N_B V_N$. Our calculations included both many-body effects and relaxation of excited states in determining the strain susceptibility of ZPL. Our findings emphasized the importance of incorporating many-body contributions in studies of optical spectroscopy under strain. Additionally, we analyzed the different signs of strain response susceptibility through molecular orbital theory, after identifying the primary molecular orbitals responding to strain.

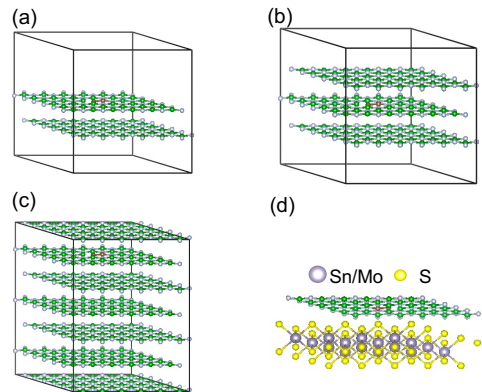


FIG. 4: Lattice structures of (a) defect in double-layer hBN, (b) defect in three-layer hBN, (c) defect in bulk hBN, (d) defect in monolayer hBN on MoS_2 and SnS_2 substrates.

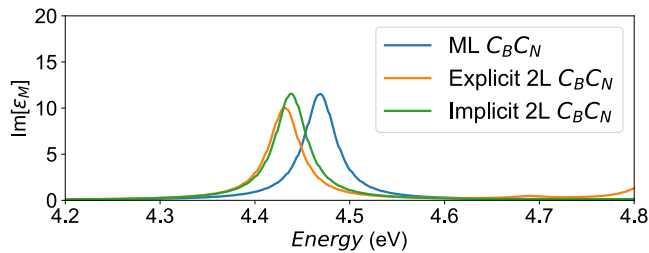
C. Layer Thickness Dependence and Substrate Effect

We next look at the layer thickness dependence and substrate effects on defect emitter properties. We use our implicit χ_{eff} -sum method [46, 47] to calculate properties of one isolated defect within 1-3 layers (Fig.4(a-b)) and bulk hBN (Fig.4(c)). We choose the AA' stacking structure and set the inter-layer distance to the bulk value of of 3.33 Å [56]. For the substrate effect study, we choose two different transition metal dichalcogenides (TMD) materials as substrates (Fig.4(d)) with layer distance to defective hBN 3.31 Å for SnS_2 and 3.33 Å for MoS_2 substrates [46].

To validate the result from our implicit χ_{eff} -sum method [46, 47], we compare its results with explicit bilayer calculations by using $C_B C_N$ in hBN as an example. In Fig.5, the panel above is the BSE absorption spectrum of defect-related peaks, where we show the explicit (orange) and implicit (green) two-layer calculations give similar results for carbon-dimer defect, which are both red-shifted by 0.03 eV compared to the monolayer one (blue). The table below summarizes the excitation energy (E_{BSE}), electronic gap (E_{GW}), and radiative lifetime (τ_R) of the defect emitter, calculated from explicit and implicit interface methods.

We then show the results of layer thickness and substrate effects on optical spectra by using implicit χ_{eff} -sum method in Fig.6 (a) and (c). With increasing the number of layers or adding substrates, the position of defect peaks remains nearly constant, with tiny shift (within 80 meV). The radiative lifetime (τ_R) also has negligible change. This result is consistent with experimental observations, where defect emitters did not change its ZPL energy either from 1L to 5L or with various substrates [57].

In Fig.6(b) and (d) we show the layer thickness and



	$E_{\text{BSE}}(\text{eV})$	τ_R (ns)	$E_{\text{GW}}(\text{eV})$	$E_b(\text{eV})$
ML	4.469	1.1	6.336	1.867
Implicit	4.438	1.3	6.045	1.607
Explicit	4.431	1.3	5.958	1.527
Error(Im.-Ex.)	0.007	< 0.01	0.087	0.080

FIG. 5: Benchmark calculations of $C_{\text{B}C_{\text{N}}}$ in two-layer hBN for χ_{eff} -sum implicit method. The figure above shows the absorption spectra at BSE. The table below listed the BSE defect peak transition energy (E_{BSE}), radiative lifetime (τ_R), electronic energy gap between defect states at GW@PBE level (E_{GW}), and exciton binding energy of the defect peak (E_b). The errors (Error) are the difference of results obtained by implicit and explicit methods. We noticed there is an error cancellation between E_{GW} and E_b .

substrate effect on GW energy gap (E_{GW}) and exciton binding energy (E_b) of intra-defect transitions. A monotonic decrease of both E_{GW} and E_b has been observed as increasing layer thickness, where the change nearly cancels each other, leaving the optical excitation energy unchanged ($E_{\text{opt}} = E_{\text{GW}} - E_b$). Interestingly, the substrate/layer effects on two defect emitters are similar; e.g. for $C_{\text{B}C_{\text{N}}}$, E_{GW} decreases by 1.348 eV from monolayer to bulk, and for $N_{\text{B}V_{\text{N}}}$ it decreases by 1.370 eV. This finding indicates that the defect state energy renormalization by layer thickness and substrates weakly depends on the specific defects, but is mostly determined by the host environment.

We then qualitatively show that the energy renormalization of E_{GW} and E_b of defects is directly related to the environmental dielectric screening surrounding the defects, represented by total 2D effective polarizability ($\alpha_{2D,\text{tot}}$) [58, 59]. $\alpha_{2D,\text{tot}}$ can be calculated by summing up the 2D effective polarizability from each subsystem ($\alpha_{2D,\text{tot}} = \alpha_{2D,\text{def}} + \alpha_{2D,\text{sub}}$; “sub” denotes substrate and “def” denotes defected hBN monolayer), where the 2D effective polarizability of the subsystem is obtained by $\alpha_{2D} = (\epsilon - 1) \cdot L / (4\pi)$. Here L is the supercell lattice constant along the out-of-plane direction, and ϵ_{sub} is the in-plane component of macroscopic dielectric tensor of the substrate calculated by Density Functional Perturbation Theory (DFPT) [60] (The dielectric constants are listed in SI). We then use equation $E = A / \alpha_{2D,\text{tot}} + C$ to fit the relation between $\alpha_{2D,\text{tot}}$ and E_{GW}/E_b , with A and C the fitting parameters. The results are plotted in

Fig.6(e), which shows the inversely proportional relation can well describe the E_{GW} and E_b dependence on environmental screening surrounding the defects (from both host hBN and substrates).

To better understand the insensitivity of defect optical transition towards environmental screening, we present an analytic model for analyzing the renormalization of the defects’ exciton binding energy (E_b). Our analysis suggests that the stability of the defect spectroscopic peak position against the layer thickness and substrate is a result of two factors: (i) the high localization of the defect wave function and (ii) the defect-related optical transition with no mixing with other transition involving delocalized wave function from the host, as discussed in detail below.

We start with the Hamiltonian for Bethe-Salpeter equation in Wannier basis [61]:

$$H^S(cv, c'v', \vec{R}) = E_{\text{GW}}\delta_{cc'}\delta_{vv'} - W_{vv'}^{cc'}(\vec{R}) + 2\delta_{S0} \sum_{\vec{R}'} \bar{V}_{v'c'}^{cv}(\vec{R}')\delta_{\vec{R}\vec{R}0} \quad (4)$$

where v/c are the pairs of occupied and unoccupied states, \vec{R} is the real-space lattice site, S is the spin, W is the screened exchange interaction between electron and hole (the direct term), \bar{V} is the exchange term from the Hartree potential, and E_{GW} is the GW electronic energy gap between c and v states. The Wannier function basis is obtained from the Fourier Transform of the reciprocal-space Kohn Sham wave function to the real-space lattice :

$$a_{v/c}(\vec{x} - \vec{R}) = \frac{1}{G^{3/2}} \sum_k e^{-i\vec{k}\cdot\vec{R}} \phi_{v/c,k}(\vec{x}) \quad (5)$$

The exciton energy and wavefunctions are obtained by diagonalizing the Hamiltonian:

$$\sum_{c'v'} H^s(cv, c'v')\phi_\lambda(c'v') = E_\lambda\phi_\lambda(cv) \quad (6)$$

where ϕ_λ is the of exciton wavefunction and E_λ is the exciton energy.

We consider the perturbation from the dielectric screening of pristine substrates or other pristine host material layers. (Notice that the in-homogeneous local dielectric environment from the host material around the defect is part of the unperturbed Hamiltonian.) The first order perturbed change to the exciton energy E_λ is then:

$$\begin{aligned} \Delta E_\lambda &= \langle \phi_\lambda | \delta \hat{H}^s | \phi_\lambda \rangle \\ &= \sum_{cv} \sum_{c'v'} \langle \phi_\lambda | cv \rangle \langle cv | \delta \hat{H}^s | c'v' \rangle \langle c'v' | \phi_\lambda \rangle \end{aligned} \quad (7)$$

where the matrix element of perturbed Hamiltonian is:

$$\begin{aligned} \langle cv | \delta \hat{H}^s | c'v' \rangle &= \delta H^S(c, v, c', v') \\ &= \delta E_{\text{GW}}^{c,v} \delta_{c,c'} \delta_{v,v'} - \delta W_{vv'}^{cc'} \end{aligned} \quad (8)$$

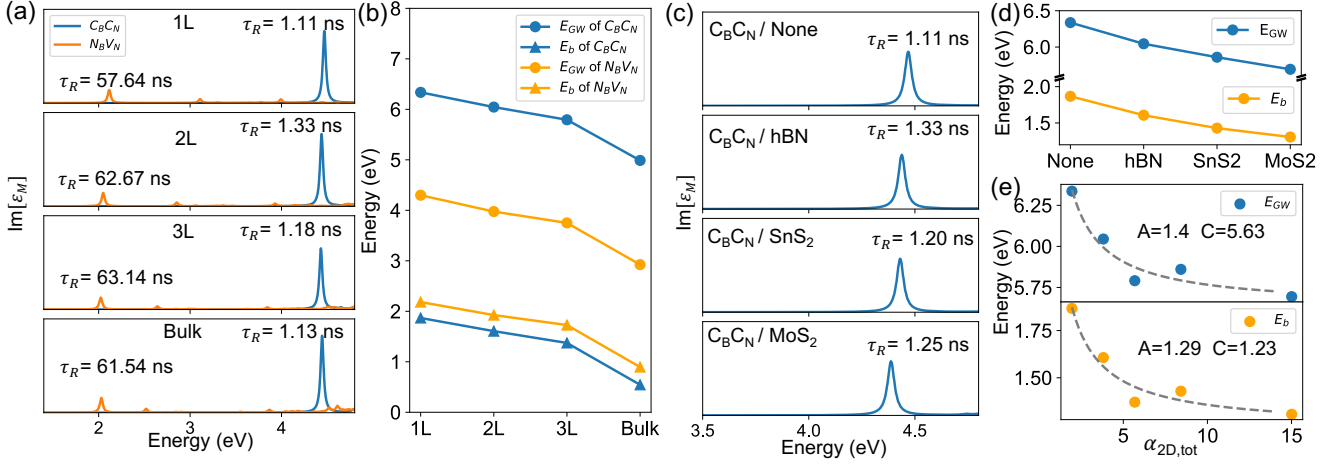


FIG. 6: Layer thickness and substrate effect on electronic and optical properties. (a) The BSE peak of $C_B C_N$ and $N_B V_N$ defects with different layer number from 1L to bulk. (b) The exciton binding energy and GW energy of $C_B C_N$ and $N_B V_N$ defects as a function of layer thickness. (c) The BSE optical spectra of $C_B C_N$ defect in monolayer hBN on various substrate. (d) The exciton binding energy and GW energy gap of $C_B C_N$ defect in monolayer hBN on different substrates. (e) The GW energy and exciton binding energy as the function of total 2D polarizability ($\alpha_{2D,tot}$). The grey dashed line is the fitting result.

in which the first term is the renormalization of electronic gap between the pair of c/v states. The second term is the change of screened exchange interaction, which contributes to the exciton binding energy change δE_b , defined as follows:

$$\begin{aligned} \delta E_b &= \langle \phi_\lambda | \delta W | \phi_\lambda \rangle \\ &= \sum_{cv} \sum_{c'v'} \langle \phi_\lambda | cv \rangle \langle cv | \delta W | c'v' \rangle \langle c'v' | \phi_\lambda \rangle. \end{aligned} \quad (9)$$

Since the exchange term from the Hartree potential \bar{V} does not depend on dielectric screening, it does not appear in the perturbative Hamiltonian.

Here we consider defect related Frenkel-like excitons, whose wavefunctions usually have components only from defect states, i.e. the $\langle \phi_\lambda | cv \rangle$ is nonzero only when c and v are defect states. The previous study on the GW band gap renormalization effect of dielectric screening on benzene systems [62] (with COHSEX model) has suggest that, when $\delta W(\vec{x}, \vec{x}')$ is smooth and slowly varying over the spacial extension of the orbital, the GW energy gap renormalization can be approximated by $\delta E_{GW}^{c,v} = P_v + P_c$, where $P_{c/v}$ is the static polarization integral for c/v state,

$$\begin{aligned} P_{c/v} &= \frac{1}{2} \int d\vec{x} \int d\vec{x}' a_{c/v}(\vec{x}) a_{c/v}^*(\vec{x}') \\ &\quad \delta W(\vec{x}, \vec{x}') a_{c/v}(\vec{x}') a_{c/v}^*(\vec{x}). \end{aligned} \quad (10)$$

When defect orbitals are highly localized in real space, the integration can be reduce to the classical limit, where $P_{c/v} = \lim_{\rho \rightarrow 0} \delta W(\rho)$ [62, 63].

The same argument can be applied to the second term in Eq. 7, where the matrix element of two particle screened Coulomb interaction change can be written as

$$\begin{aligned} \delta W_{vv'}^{cc'}(\vec{R}) &= \int_{U.C.} d\vec{x} \int_{U.C.} d\vec{x}' a_c^*(\vec{x}) a_{c'}(\vec{x}) \\ &\quad \delta W(\vec{x} + \vec{R}, \vec{x}') a_v(\vec{x}') a_{v'}^*(\vec{x}'). \end{aligned} \quad (11)$$

Since a single defect is not subject to a spacial periodicity, we can ignore the inter-site interaction and set $\vec{R}=0$. Then we rewrite the equation with two-electrons' distance $\rho = |\vec{x} - \vec{x}'|$, assuming the substrate screening being homogeneous in-plane (which is a reasonable approximation according to our past work [46]),

$$\begin{aligned} \delta W_{vv'}^{cc'} &= \int_{U.C.} d\vec{x} \int_{U.C.} d\vec{x}' a_c^*(\vec{x}) a_{c'}(\vec{x}) \\ &\quad \delta W(\rho) a_v(\vec{x}') a_{v'}^*(\vec{x}'). \end{aligned} \quad (12)$$

Given localized (Frenkel) exciton, ρ is rather small or exciton wavefunction is spatially confined. With orthonormal condition of single-particle wavefunctions, we have

$$\begin{aligned} \delta W_{vv'}^{cc'} &\approx \lim_{\rho \rightarrow 0} \delta W(\rho) \int_{U.C.} d\vec{x} \int_{U.C.} d\vec{x}' \\ &\quad a_c^*(\vec{x}) a_{c'}(\vec{x}) a_v(\vec{x}') a_{v'}^*(\vec{x}') \\ &= \lim_{\rho \rightarrow 0} \delta W(\rho) \delta_{c,c'} \delta_{v,v'} \end{aligned} \quad (13)$$

Combining the discussions above on both terms in Eq.8, we have the $\langle cv | \delta \hat{H}^s | c'v' \rangle = 0$ when c and v are both defect single-particle states. Thus, the Frenkel-like exciton, composed by localized defect-defect transitions, will experience no change at presence of substrate screening.

At last, we apply a static model for $\delta W(\vec{x}, \vec{x}')$ derived from image charges [63] and compare with *ab-initio* GW/BSE results. The environmental screening potential can be modeled as the potential energy of two charges in the defect layer (with dielectric constant ϵ_{def}) on top of substrate (with dielectric constant ϵ_{sub}) [63]. We assume the region above the defect layer to be a vacuum.

$$W(\vec{x}, \vec{x}') = W(\rho) = \frac{1}{\epsilon_{def}\rho} + 2 \sum_{n=1}^{\infty} \frac{L_{12}^n}{\epsilon\{\rho^2 + (2nd)^2\}^{1/2}} + L_{12} \sum_{n=0}^{\infty} \frac{L_{12}^n}{\epsilon(\rho^2 + [(2n+1)d]^2)^{1/2}} \quad (14)$$

where d is the thickness of the defect layer, and $L_{12} = (\epsilon_{def} - \epsilon_{sub})/(\epsilon_{def} + \epsilon_{sub})$. We use the monolayer defect system without any substrate ($\epsilon_{sub} = 1$) as the reference, then δW is defined as the change of W with and without substrates:

$$\delta W(\rho, \epsilon_{sub}) = W(\rho, \epsilon_{sub}) - W(\rho, \epsilon_{sub} = 1). \quad (15)$$

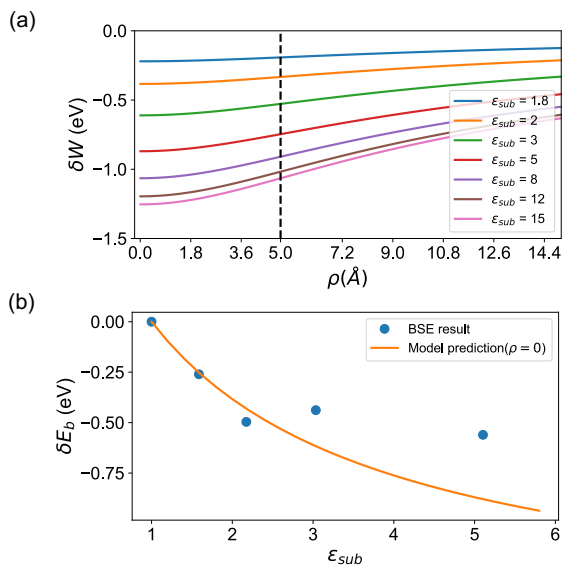


FIG. 7: (a) The change of screened Coulomb potential as a function of electron-hole separation (ρ) at different substrate dielectric constants ϵ_{sub} . The calculation is performed using Eq. 14 and Eq. 15. The dash line shows the localization range of defect wave function where 99% of density lies within 5 Å. (b) The δE_b comparison of model prediction by using Eq. 9, Eq. 14, and Eq. 15 with results from full *ab-initio* BSE. Good agreement between BSE results (blue dots) and model prediction (orange line) is obtained in the relatively low substrate dielectric constant range. In this range, δW varies slower, better satisfying the approximation in Eq. 12.

We plotted the change of screened Coulomb potential,

$\delta W(\rho, \epsilon_{sub})$ in Fig. 7 (a), where the defect layer thickness $d = 6.66\text{Å}$ is extracted from inter-layers distance, and defect layer dielectric constant ϵ_{def} is obtained in SI section V. The dashed line at 5 Å represents the maximum spanning range of the localized defect states $1b_1$ and $2b_1$.

Fig. 7(b) shows that the δE_b calculated by Eq. 9, Eq. 14, and Eq. 15 compares reasonably well with *ab-initio* BSE calculations (blue dots), especially in low substrate screening regime. The underestimation of δE_b at the high dielectric constant of substrates ϵ_{sub} range may be due to an over-simplification of model W in Eq. 14. Nevertheless, the full *ab-initio* GW/BSE calculation suggests that the cancellation effect for defect state transitions between exciton binding energy (δE_b) and GW quasiparticle energy renormalization (δE_{GW}) still holds even at high substrate dielectric screening.

IV. CONCLUSIONS

In this work, we have explored the impact of strain, layer thickness, and substrate effects on the electronic and optical properties of point defects in 2D insulator-hexagonal boron nitride (hBN). Our investigation takes into account the effects of many-body interaction and excited-state relaxation. We first analyzed various contributions to strain susceptibility of ZPL, and found the dominant contributions often stem from the changes at the single-particle level. We explained the ZPL shift direction under strain through molecular orbital theory, which is defect dependent, relying on the chemical bonding nature at the defect center.

Next our *ab-initio* calculations demonstrate the robustness of optical peak position of defect single photon emitters (SPEs) when varying number of layers and substrates. We reveal the perfect cancellation between the renormalization of quasiparticle energy gap and exciton binding energy due to environmental screening. To further understand this result, we derived analytical models based on solving BSE with Wannier basis for Frenkel excitons, to reveal the underlying mechanism and the required condition, i.e. the localization nature of defect bound exciton. We then use simple image-charge model for screened Coulomb potential to further validate such cancellation effect.

Our findings provide in-depth insights of mechanism and conditions that control the environmental impact on the properties of quantum defects, and shine light on the emerging research on strain and substrate engineering of quantum defects in 2D materials.

ACKNOWLEDGMENTS

We acknowledge the support by the National Science Foundation under grant no. DMR-2143233. This research used resources of the Scientific Data and Com-

puting center, a component of the Computational Science Initiative, at Brookhaven National Laboratory under Contract No. DE-SC0012704, the lux supercomputer at UC Santa Cruz, funded by NSF MRI grant AST 1828315, the National Energy Research Scientific Com-

puting Center (NERSC) a U.S. Department of Energy Office of Science User Facility operated under Contract No. DE-AC02-05CH11231, the Extreme Science and Engineering Discovery Environment (XSEDE) which is supported by National Science Foundation Grant No. ACI-1548562 [64].

-
- [1] I. Aharonovich and M. Toth, *Sci.* **358**, 170 (2017).
- [2] X. Liu and M. C. Hersam, *Nat. Rev. Mater.* **4**, 669 (2019).
- [3] G. Wolfowicz, F. J. Heremans, C. P. Anderson, S. Kanai, H. Seo, A. Gali, G. Galli, and D. D. Awschalom, *Nat. Rev. Mater.* **6**, 906 (2021).
- [4] D. Yim, M. Yu, G. Noh, J. Lee, and H. Seo, *ACS Appl. Mater. Interfac.* **12**, 36362 (2020).
- [5] S. Li, J.-P. Chou, A. Hu, M. B. Plenio, P. Udvarhelyi, G. Thiering, M. Abdi, and A. Gali, *npj Quantum Inf.* **6**, 1 (2020).
- [6] N. Mendelson, M. Doherty, M. Toth, I. Aharonovich, and T. T. Tran, *Advanced Materials* **32**, 1908316 (2020).
- [7] T. T. Tran, K. Bray, M. J. Ford, M. Toth, and I. Aharonovich, *Nat. Nanotechnol.* **11**, 37 (2016).
- [8] A. Gottscholl, M. Kianinia, V. Soltamov, S. Orlinkii, G. Mamin, C. Bradac, C. Kasper, K. Krambrock, A. Sperlich, M. Toth, *et al.*, *Nat. Mater.* **19**, 540 (2020).
- [9] A. Gottscholl, M. Diez, V. Soltamov, C. Kasper, A. Sperlich, M. Kianinia, C. Bradac, I. Aharonovich, and V. Dyakonov, *Sci. Adv.* **7**, eabf3630 (2021).
- [10] X. Gao, S. Vaidya, K. Li, P. Ju, B. Jiang, Z. Xu, A. E. L. Alleca, K. Shen, T. Taniguchi, K. Watanabe, *et al.*, arXiv preprint arXiv:2203.13184 (2022).
- [11] C. Qian, V. Villafañe, M. Schalk, G. V. Astakhov, U. Kentsch, M. Helm, P. Soubelet, N. P. Wilson, R. Rizzato, S. Mohr, *et al.*, arXiv preprint arXiv:2202.10980 (2022).
- [12] J. R. Reimers, J. Shen, M. Kianinia, C. Bradac, I. Aharonovich, M. J. Ford, and P. Piecuch, *Phys. Rev. B* **102**, 144105 (2020).
- [13] V. Ivády, G. Barcza, G. Thiering, S. Li, H. Hamdi, J.-P. Chou, Ö. Legeza, and A. Gali, *npj Comput. Mater.* **6**, 1 (2020).
- [14] G. Grosso, H. Moon, B. Lienhard, S. Ali, D. K. Efetov, M. M. Furchi, P. Jarillo-Herrero, M. J. Ford, I. Aharonovich, and D. Englund, *Nat. Commun.* **8**, 705 (2017).
- [15] N. Mendelson, D. Chugh, J. R. Reimers, T. S. Cheng, A. Gottscholl, H. Long, C. J. Mellor, A. Zettl, V. Dyakonov, P. H. Beton, *et al.*, *Nat. Mater.* **20**, 321 (2021).
- [16] R. Bourrellier, S. Meuret, A. Tararan, O. Stéphan, M. Kociak, L. H. Tizei, and A. Zobelli, *Nano Lett.* **16**, 4317 (2016).
- [17] L. Museur, E. Feldbach, and A. Kanaev, *Phys. Rev. B* **78**, 155204 (2008).
- [18] M. E. Turiansky, A. Alkauskas, L. C. Bassett, and C. G. Van de Walle, *Phys. Rev. Lett.* **123**, 127401 (2019).
- [19] A. Sajid and K. S. Thygesen, *2D Mater.* **7**, 031007 (2020).
- [20] M. Fischer, J. Caridad, A. Sajid, S. Ghaderzadeh, M. Ghorbani-Asl, L. Gammelgaard, P. Bøggild, K. S. Thygesen, A. Krasheninnikov, S. Xiao, *et al.*, *Sci. Adv.* **7**, eabe7138 (2021).
- [21] C. Jara, T. Rauch, S. Botti, M. A. Marques, A. Norambuena, R. Coto, J. Castellanos-Aéguila, J. R. Maze, and F. Muñoz, *J. Phys. Chem. A* **125**, 1325 (2021).
- [22] K. Li, T. J. Smart, and Y. Ping, *Phys. Rev. Mater.* **6**, L042201 (2022).
- [23] O. Golami, K. Sharman, R. Ghobadi, S. C. Wein, H. Zadeh-Haghighi, C. G. da Rocha, D. R. Salahub, and C. Simon, *Phys. Rev. B* **105**, 184101 (2022).
- [24] M. Maciaszek, L. Razinkovas, and A. Alkauskas, *Phys. Rev. Mater.* **6**, 014005 (2022).
- [25] M. Mackoiti-Sinkevičienė, M. Maciaszek, C. G. Van de Walle, and A. Alkauskas, *Appl. Phys. Lett.* **115**, 212101 (2019).
- [26] A. Vokhmintsev, I. Weinstein, and D. Zamyatin, *J. Lumin.* **208**, 363 (2019).
- [27] H. Hamdi, G. Thiering, Z. Bodrog, V. Ivády, and A. Gali, *npj Comput. Mater.* **6**, 1 (2020).
- [28] S. Li, A. Pershin, G. Thiering, P. Udvarhelyi, and A. Gali, *J. Phys. Chem. Lett.* **13**, 3150 (2022).
- [29] T. T. Tran, C. Elbadawi, D. Totonjian, C. J. Lobo, G. Grosso, H. Moon, D. R. Englund, M. J. Ford, I. Aharonovich, and M. Toth, *ACS nano* **10**, 7331 (2016).
- [30] M. Krečmarová, R. Canet-Albiach, H. Pashaei-Adl, S. Gorji, G. Muñoz-Matutano, M. Nesládek, J. P. Martínez-Pastor, and J. F. Sánchez-Royo, *ACS Appl. Mater. Interfac.* **13**, 46105 (2021).
- [31] F. Wu, T. J. Smart, J. Xu, and Y. Ping, *Phys. Rev. B* **100**, 081407(R) (2019).
- [32] P. Dev, arXiv preprint arXiv:2002.05098 (2020).
- [33] Y. Ping and T. J. Smart, *Nat Comput Sci* **1**, 646 (2021).
- [34] D. Amblard, G. D’Avino, I. Duchemin, and X. Blase, arXiv:2204.11671 [cond-mat] (2022), arXiv:2204.11671 [cond-mat].
- [35] D. Wang and R. Sundararaman, *Phys. Rev. B* **101**, 054103 (2020).
- [36] D. Wang and R. Sundararaman, *Phys. Rev. Materials* **3**, 083803 (2019).
- [37] P. Giannozzi, S. Baroni, N. Bonini, M. Calandra, R. Car, C. Cavazzoni, D. Ceresoli, G. L. Chiarotti, M. Cococcioni, I. Dabo, A. Dal Corso, S. de Gironcoli, S. Fabris, G. Fratesi, R. Gebauer, U. Gerstmann, C. Gougoussis, A. Kokalj, M. Lazzeri, L. Martin-Samos, N. Marzari, F. Mauri, R. Mazzarello, S. Paolini, A. Pasquarello, L. Paulatto, C. Sbraccia, S. Scandolo, G. Sclauzero, A. P. Seitsonen, A. Smogunov, P. Umari, and R. M. Wentzcovitch, *J. Phys.: Condens. Matter* **21**, 395502 (2009).
- [38] J. P. Perdew, K. Burke, and M. Ernzerhof, *Phys. Rev. Lett.* **77**, 3865 (1996).
- [39] M. Schlipf and F. Gygi, *Computer Physics Communications* **196**, 36 (2015).
- [40] D. R. Hamann, *Phys. Rev. B* **88**, 085117 (2013).
- [41] T. J. Smart, K. Li, J. Xu, and Y. Ping, *npj Comput Mater* **7**, 1 (2021).

- [42] Y. Ping, D. Rocca, and G. Galli, *Chem. Soc. Rev.* **42**, 2437 (2013).
- [43] A. Marini, C. Hogan, M. Grüning, and D. Varsano, *Computer Physics Communications* **180**, 1392 (2009).
- [44] C. A. Rozzi, D. Varsano, A. Marini, E. K. U. Gross, and A. Rubio, *Phys. Rev. B* **73**, 205119 (2006).
- [45] F. Wu, D. Rocca, and Y. Ping, *J. Mater. Chem. C* **7**, 12891 (2019).
- [46] C. Guo, J. Xu, D. Rocca, and Y. Ping, *Phys. Rev. B* **102**, 205113 (2020).
- [47] C. Guo, J. Xu, and Y. Ping, *J. Phys.: Condens. Matter* **33**, 234001 (2021).
- [48] M. Mackoīt-Sinkevičienė, M. Maciaszek, C. G. Van de Walle, and A. Alkauskas, *Appl. Phys. Lett.* **115**, 212101 (2019).
- [49] F. Wu, T. J. Smart, J. Xu, and Y. Ping, *Phys. Rev. B* **100**, 081407 (2019).
- [50] M. Winter, M. H. E. Bousquet, D. Jacquemin, I. Duchemin, and X. Blase, *Phys. Rev. Materials* **5**, 095201 (2021).
- [51] M. Abdi, J.-P. Chou, A. Gali, and M. B. Plenio, *ACS Photonics* **5**, 1967 (2018).
- [52] S. Gao, H.-Y. Chen, and M. Bernardi, *npj Comput Mater* **7**, 85 (2021).
- [53] F. Hayee, L. Yu, J. L. Zhang, C. J. Ciccarino, M. Nguyen, A. F. Marshall, I. Aharonovich, J. Vučković, P. Narang, T. F. Heinz, and J. A. Dionne, *Nat. Mater.* **19**, 534 (2020).
- [54] G. Grosso, H. Moon, B. Lienhard, S. Ali, D. K. Efetov, M. M. Furchi, P. Jarillo-Herrero, M. J. Ford, I. Aharonovich, and D. Englund, *Nat Commun* **8**, 705 (2017).
- [55] Y. Xue, H. Wang, Q. Tan, J. Zhang, T. Yu, K. Ding, D. Jiang, X. Dou, J.-j. Shi, and B.-q. Sun, *ACS Nano* **12**, 7127 (2018).
- [56] O. Hod, *J. Chem. Theory Comput.* **8**, 1360 (2012).
- [57] M. Krečmarová, R. Canet Albiach, H. Pashaei Adl, S. Gorji, G. Muñoz-Matutano, M. Nesladek, J. Martínez-Pastor, and J. F. Sánchez Royo, *ACS Applied Materials & Interfaces* **13**, 46105 (2021).
- [58] A. Molina-Sánchez, G. Catarina, D. Sangalli, and J. Fernández-Rossier, *J. Mater. Chem. C* **8**, 8856 (2020).
- [59] T. Tian, D. Scullion, D. Hughes, L. H. Li, C.-J. Shih, J. Coleman, M. Chhowalla, and E. J. G. Santos, *Nano Lett.* **20**, 841 (2020).
- [60] S. Baroni, S. de Gironcoli, A. Dal Corso, and P. Gianozzi, *Rev. Mod. Phys.* **73**, 515 (2001).
- [61] F. Bechstedt, *Many-Body Approach to Electronic Excitations*, Springer Series in Solid-State Sciences, Vol. 181 (Springer Berlin Heidelberg, Berlin, Heidelberg, 2015).
- [62] J. B. Neaton, M. S. Hybertsen, and S. G. Louie, *Phys. Rev. Lett.* **97**, 216405 (2006).
- [63] Y. Cho and T. C. Berkelbach, *Phys. Rev. B* **97**, 041409 (2018).
- [64] J. Towns, T. Cockerill, M. Dahan, I. Foster, K. Gauthier, A. Grimshaw, V. Hazlewood, S. Lathrop, D. Lifka, G. D. Peterson, R. Roskies, J. R. Scott, and N. Wilkins-Diehr, *Comput. Sci. Eng.* **16**, 62 (2014).

Supplementary Materials: Effect of Environmental Screening and Strain on Optoelectronic Properties of Two-Dimensional Quantum Defects

Shimin Zhang and Kejun Li

Department of Physics, University of California, Santa Cruz, CA, 95064, USA

Chunhao Guo and Yuan Ping*

Department of Chemistry and Biochemistry, University of California, Santa Cruz, CA, 95064, USA

I. NUMERICAL CONVERGENCE OF GW/BSE CALCULATIONS

Fig.S1 summarizes GW convergence tests using $C_B C_N$ in hBN as an example. In Fig.S1(a) we show the band number $BndsRnXp = 1800$ and dielectric function block size of 8 Ry converge quasiparticle energies up to 50 meV. Fig. S1(b) shows that a vacuum size of 33.5 Bohr is sufficient, where the Coulomb truncation is utilized to accelerate the convergence [?]. Lastly, the wave function cutoff energy of 30 Ry is chosen for GW self-energy as shown in Fig. S1(c).

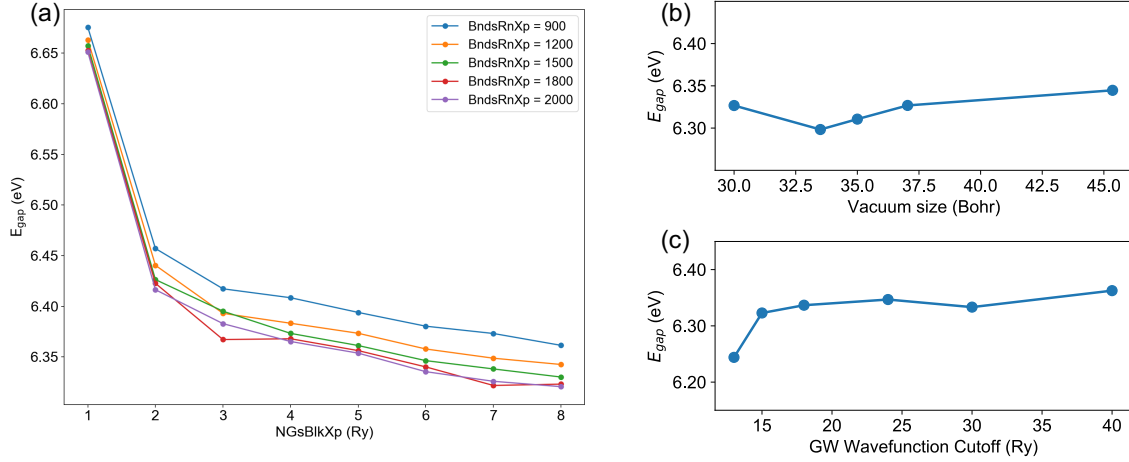


FIG. S1: GW convergence tests of HOMO-LUMO gap E_{gap} of $C_B C_N$ defect in hBN, with respect to (a) the number of bands ($BndsRnXp$) and response block size ($NGSBlkXp$) for the dielectric matrix, (b) vacuum size, and (c) energy cutoff of dielectric matrix and GW self-energy.

Fig. S2 (a) shows the BSE spectrum is converged at bands chosen for the BSE kernel from 100 to 180 (43 unoccupied and 37 occupied bands) and the BSE Kernel size of 5 Ry. Fig.S2 (b) shows the BSE spectrum with respect to the total number of bands chosen for dielectric matrices in the screened Coulomb potential.

II. BSE SPECTRUM OF $C_B C_N$ AND $N_B V_N$ DEFECTS IN hBN

$C_B C_N$ defect in hBN - Fig. S3(a) shows the BSE spectrum of $C_B C_N$ in monolayer hBN, which has a sharp peak at 4.44 eV for defect state transition. The related exciton wave function is highly localized around the carbon defect center, as shown in Fig. S3(b).

$N_B V_N$ defect in hBN - Fig.S4 shows the BSE spectrum and exciton wave functions of three defect-transition related peaks for $N_B V_N$. The BSE spectrum in Fig. S4(a) labeled the three peaks as A,B,C, which are related

*Electronic address: yuanping@ucsc.edu

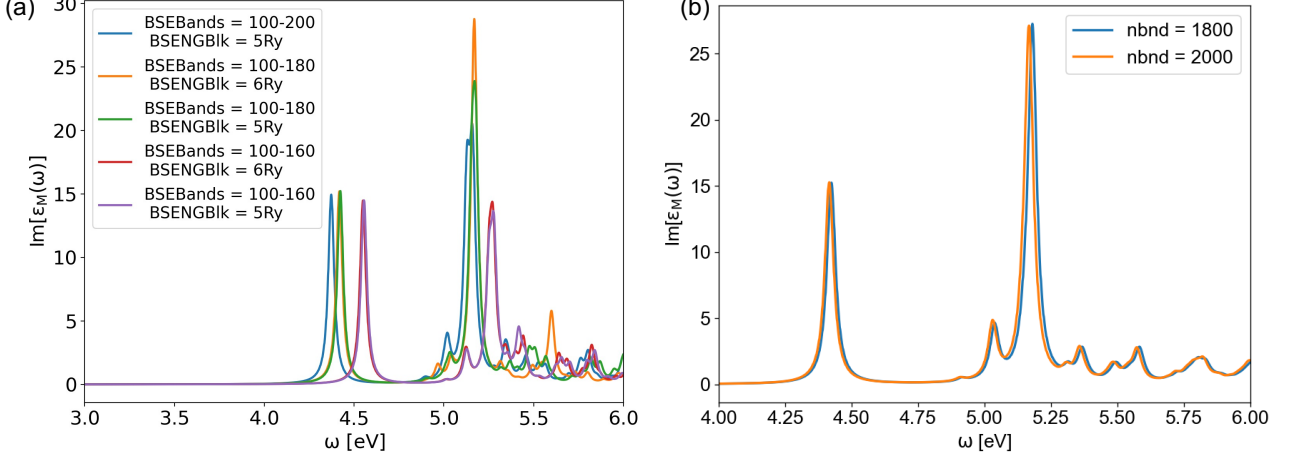


FIG. S2: The $C_B C_N$ BSE spectrum convergence test of $C_B C_N$, with respect to (a) bands used to construct the electron-hole pair wave function in BSE (BSEBands) and screened interaction block size (BSENGBlk), and (b) number of bands in GW level calculation for dielectric function (nbnd).

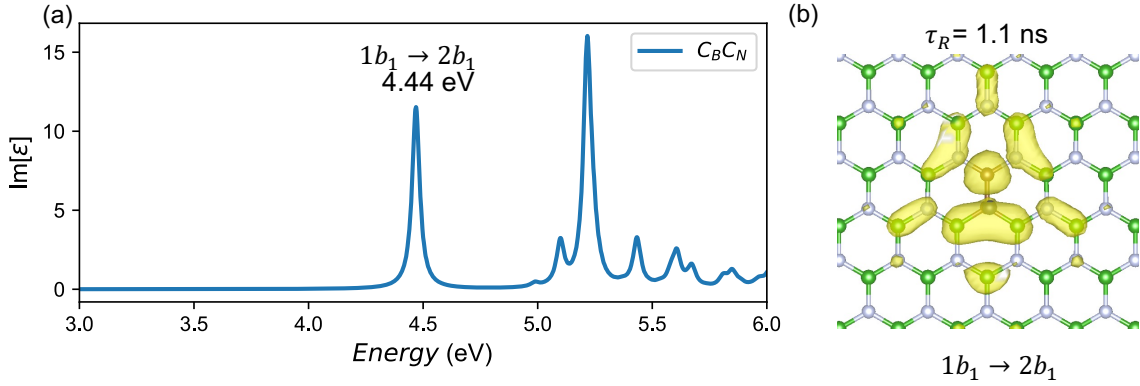


FIG. S3: (a) The BSE spectrum of $C_B C_N$ in hBN. (b) The exciton wave function related to the defect transition $1b_1 \rightarrow 2b_1$ in $C_B C_N$, with an isosurface level of 0.005 \AA^{-3} .

to the $1b_{1\uparrow} \rightarrow 2b_{1\uparrow}$ transition. The main defect peak A, at 2.12 eV, is of primary consideration in the main text, and its exciton wave function solely includes $1b_{1\uparrow} \rightarrow 2b_{1\uparrow}$ transition. Peaks B and C are related to the mixing of defect-defect state transition and defect-bulk state transition. The exciton wave functions are plotted with the hole fixed at the substitutional Boron atom. Since the exciton wave function of peak B and C include delocalized bulk state component besides the defect states, they are less localized than peak A, and thus more sensitive to the change of environmental dielectric screening as we pointed out in the main text.

III. THE LOW-SYMMETRY STRUCTURE AND ITS OPTICAL TRANSITIONS OF $N_B V_N$

We investigated both in-plane (C_{2v} symmetry) and out-of-plane distorted geometry (C_s symmetry) while considering both possible excited states A_1 and B'_1 , which could account for the observed SPE. We took into account both the Frank-Condon shift and many-body effect, and summarized the energy diagram of two excited states and ground state under different symmetries in Fig.S5.

Here we use multi-particle wave function label to denote the ground state and excited states. The B_1 is the ground

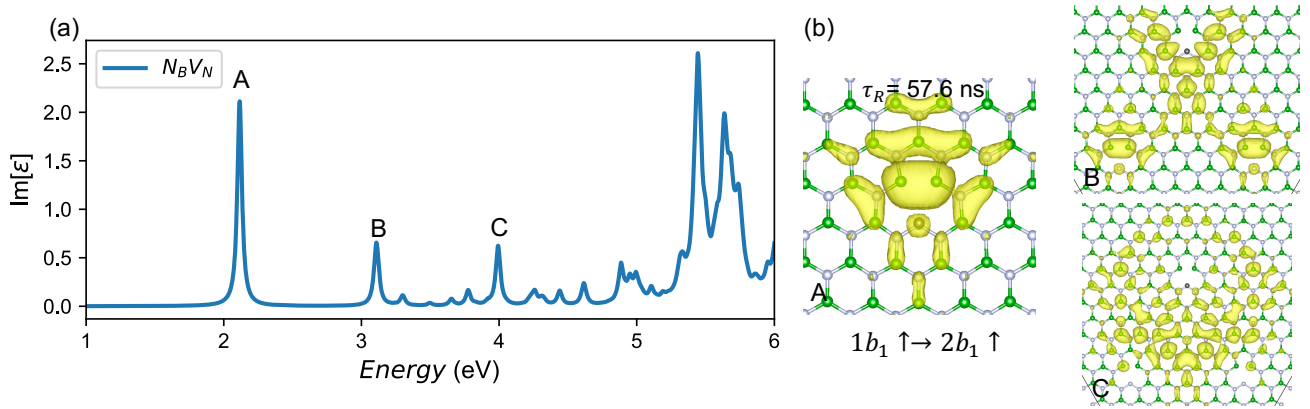


FIG. S4: (a) The BSE spectrum of $N_B V_N$ with three defect-related transitions A, B and C. (b) The three exciton wave functions related to peaks A, B, C, with the hole fixed at the substitution Boron atom and an isosurface level of 0.015 \AA^{-3} .

state with the electron configuration of $[1a_1]^2[1b_1]^1[2b_1]^0$ as shown in the main text Fig.2. The excited state A_1 corresponds to the electron configuration of $[1a_1]^1[1b_1]^2[2b_1]^0$, and B'_1 corresponds to the $[1a_1]^2[1b_1]^0[2b_1]^1$.

Fig. S5(a) shows the energy diagram of the ground state B_1 and the excited state A_1 , while Fig. S5(b) shows the ground state B_1 and the excited state B'_1 . The system is calculated under both C_{2v} and C_s symmetries, denoted in the parentheses, for all three states. The relaxation energy is calculated at the DFT level while the vertical excitation energy is calculated by GW/BSE, which is given in Fig. S6. The ground state energy is found to be 0.11 eV lower at C_s symmetry than C_{2v} , with out-of-plane distortion of 0.66 Å, consistent with the previous studies [?] [?]. On the other hand, both A_1 and B'_1 excited states have lower energy at C_{2v} symmetry. This indicates that both excited states will experience a local structural distortion from C_s to C_{2v} when excited from the C_s symmetry ground state.

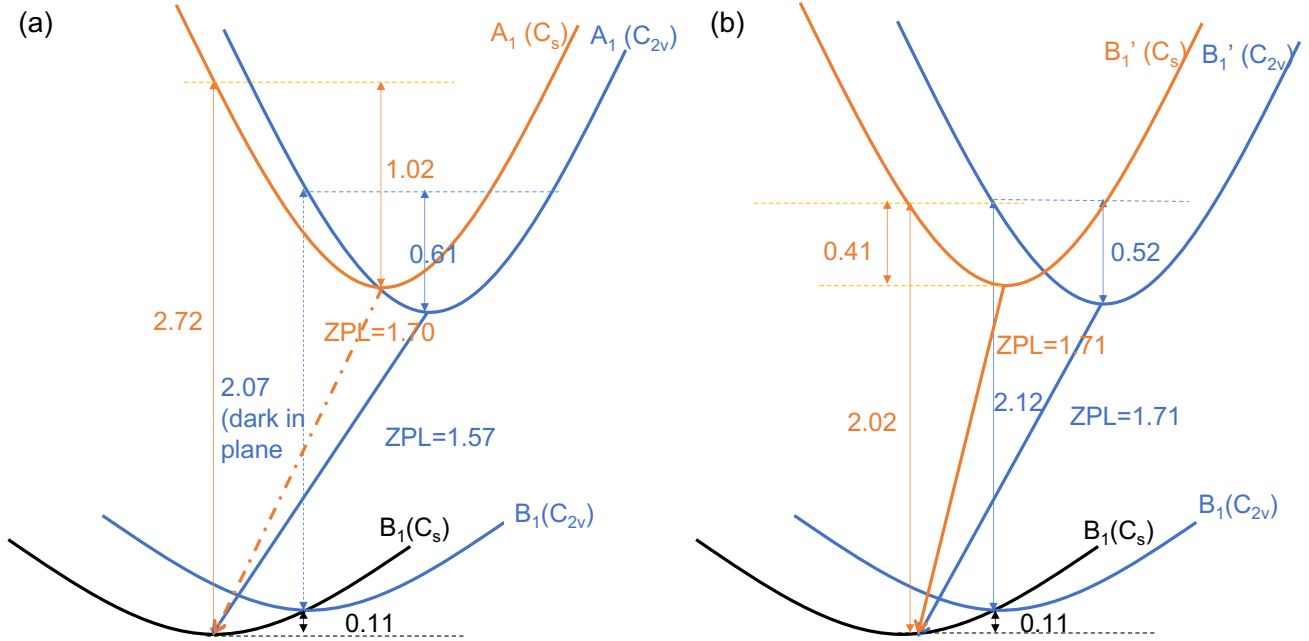


FIG. S5: The energy diagram of the transition from ground state B_1 to (a) A_1 and (b) B'_1 excited state, where C_s and C_{2v} in the parentheses denote the symmetry of the state.

The B_1 -to- A_1 transition has been the main source of SPE, since it is the lowest transition and has been estimated to have a 2 eV ZPL that lies within the experimentally observed SPE range [? ?]. Fig. S5(a) shows that at C_{2v} symmetry, the B_1 -to- A_1 transition is forbidden, but it becomes allowed as the symmetry breaks to C_s with a vertical transition energy of 2.7 eV. The details of the absorption spectrum are presented in Fig. S6, which are consistent with previous calculations at the same level of theory and the same structural symmetry [?]. The most viable optical excitation-recombination path for ZPL between B_1 and A_1 is to first excite from the C_s symmetry ground state to C_s symmetry A_1 , undergo an ~ 1 eV reorganization within $A_1(C_s)$, followed by local structural distortion to $A_1(C_{2v})$, and then optically recombine to $B_1(C_s)$. Such a path has a long reorganization path and small ZPL of 1.57 eV (listed in Fig. S6). We believe it is unlikely to provide a bright SPE peak that falls within the experimentally observed SPE range of 1.6 to 2.2 eV.

We have chosen the B_1 -to- B'_1 transition as our primary focus in our study. As depicted in the energy diagram in Fig. S5(b), this recombination process involves a shorter relaxation path for the excited state. The B'_1 excited state in the C_s and C_{2v} symmetry have similar relaxed energy, and therefore, can both contribute to an estimated ZPL of 1.7 eV.

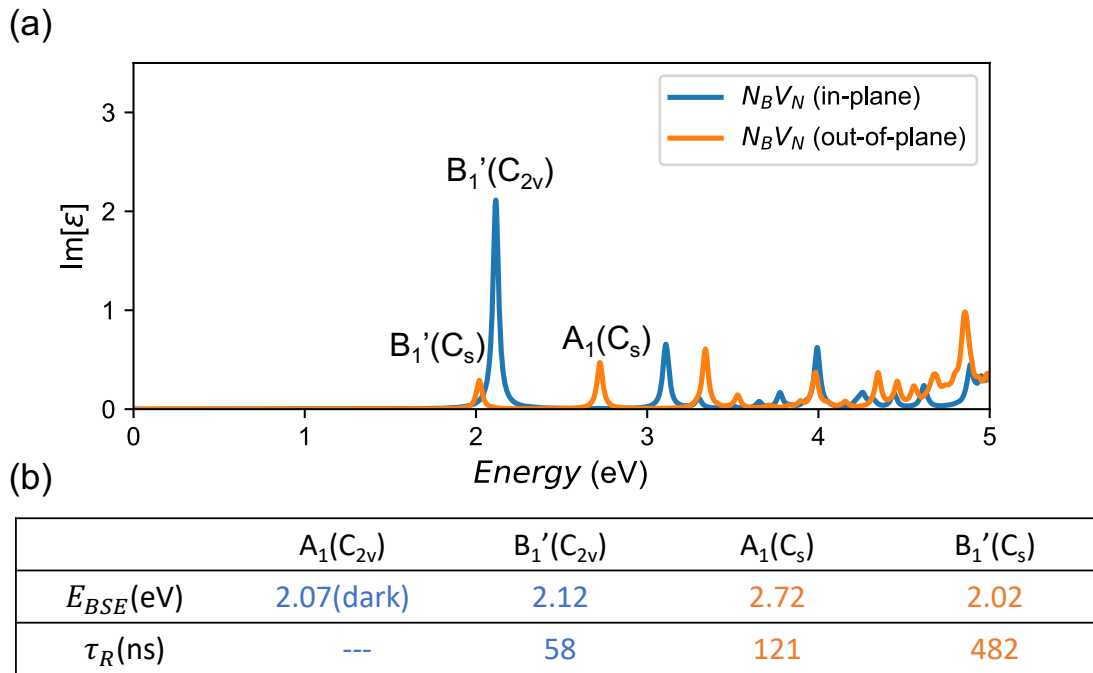


FIG. S6: (a) The BSE spectrum of $N_B V_N$ with in-plane (C_{2v} symmetry) and out-of-plane (C_s symmetry) geometry. (b) The BSE excitation energy and corresponding radiative lifetime for both structures.

IV. EXPERIMENT RESULT CONVERSION

In the experiment work we cited in main text the origin measurement of strain susceptibility is under the experimentally defined strain, which usually denote as the strain that is applied macroscopically on substrate [?] or applied by homogeneous pressure [?]. Therefore we converted the experimental data for proper comparison.

In Grosso et al's work [?] the ZPL strain susceptibility was measured as -3.1 meV, 3.3 meV, and 6 meV/% for three different emitters. These results are not directly comparable to our calculated strain susceptibilities, because their strain is applied and defined by the bending of the substrate, while our strain is defined by the stretching rate of defect layer itself. They introduced the strain transfer rate among two consecutive layers as $t \sim 98\%$. The effective strain at the emitter location is $S_{eff}^N = S_{eff}^{N-1} \cdot t = \dots = \epsilon \cdot t^N$. For number of layers $N \sim 150$ in this experiment, the local strain can be 20 times smaller than applied strain, i.e. $S_{eff} = \epsilon \cdot 0.05$. We apply this conversion relation to their experiment result and obtained the strain susceptibilities of -61 meV, 66 meV, and 120 meV/% for the three emitters, which is of the same scale as our result.

In Xue et al's work [?], 9 different SPE between 1.7-2.2 eV are investigated with external pressure. The pressure-strain conversion table provided in this paper indicates a conversion relation of -0.049% strain per 1 GPa pressure for in-plane strain. The converted strain susceptibility in TABLE.S1 is ranges from -287 meV/% to 214 meV/%. Although these values are for the biaxial strain, our calculated results fall within the appropriate scale.

TABLE S1: Measured data from experiment [?]

ZPL(eV)	2.125	2.1	2.065	2.035	2.025	1.985	1.925	1.9	1.76
Pressure coefficient (meV/Gpa)	-6.1	14.1	-4.5	2.7	-2.5	-10.3	-5.9	-3.9	-10.5
Strain susceptibility ^a (meV/strain)	124.49	-287.76	91.84	-55.1	51.0	210.2	120.41	79.59	214.29

^abiaxial strain

V. SYSTEM DIELECTRIC CONSTANT AND 2D EFFECTIVE POLARIZABILITY

The Table S2 gives the dielectric constant and 2D effective polarizability of mono-layer(ML), two layers(2L), three layers(3L) $C_B C_N$, as well as $C_B C_N$ on SnS_2 substrate($C_B C_N|SnS_2$) and MoS_2 substrate ($C_B C_N|MoS_2$). In this table the ϵ_{sub} represents the dielectric constant of substrate or other layers, $\alpha_{2D,sub}$ is the 2D effective polarizability of substrate or other layers, and $\alpha_{2D,tot}$ is the system total 2D effective polarizability.

	ML	2L	3L	$C_B C_N SnS_2$	$C_B C_N MoS_2$
$\alpha_{2D,tot}$	1.946	3.814	5.682	8.421	15.009
ϵ_{sub}	1	1.589	2.020	3.047	5.125
$\alpha_{2D,sub}$	0	1.868	3.735	6.475	13.063

TABLE S2: System total 2D effective polarizability $\alpha_{2D,tot}$, substrate dielectric ϵ_{sub} , and substrate 2D effective polarizability $\alpha_{2D,sub}$ of each $C_B C_N$ system.

The dielectric constant of 2D systems depends on the lattice length along the out-of-plane direction, denoted as L . We calculated the dielectric constant of the monolayer defective hBN system at $L = 30.00$ Bohr to be $\epsilon_{def}(L = 30.00) = 1.815$ at DFPT. In the image charge model for the screened potential change, we set the defective hBN monolayer thickness to $d = 12.59$ Bohr, twice of the bulk hBN interlayer distance. To obtain the corresponding $\epsilon_{def}(L = 12.59)$, we use the 2D effective polarizability as the bridging quantity, which is independent on the lattice length or vacuum sizes, i.e. $\alpha_{def}(L = 30) = \alpha_{def}(L = 12.59)$. Combining this with the relation between 2D effective polarizability and dielectric constant, $\alpha_{2D,def}(L) = (\epsilon_{def} - 1) \cdot L/(4\pi)$, we can determine the dielectric constant at $L = 12.59$ to be $\epsilon_{def}(L = 12.59) = 2.940$, which is used in our model calculations in the main text.